DNA-PK Inhibitor Peposertib Amplifies Radiation-Induced Inflammatory Micronucleation and Enhances TGFβ/PD-L1 Targeted Cancer Immunotherapy

Michael I. Carr[1], Li-Ya Chiu[1], Yige Guo[1], Chunxiao Xu[1], Adam S. Lazorchak[1], Huakui Yu[1], Guozhong Qin[1], Jin Qi[1], Bo Marelli[1], Yan Lan[1], Qing Sun[1], Frank Czauderna[1], Frank T. Zenke[2], Andree Blaukat[2], and Lyubomir T. Vassilev[1]

ABSTRACT

Radiotherapy is the most widely used cancer treatment and improvements in its efficacy and safety are highly sought-after. Peposertib (also known as M3814), a potent and selective DNA-dependent protein kinase (DNA-PK) inhibitor, effectively suppresses the repair of radiation-induced DNA double-strand breaks (DSB) and regresses human xenograft tumors in preclinical models. Irradiated cancer cells devoid of p53 activity are especially sensitive to the DNA-PK inhibitor, as they lose a key cell-cycle checkpoint circuit and enter mitosis with unrepaired DSBs, leading to catastrophic consequences. Here, we show that inhibiting the repair of DSBs induced by ionizing radiation with peposertib offers a powerful new way for improving radiotherapy by simultaneously enhancing cancer cell killing and response to a bifunctional TGFβ "trap"/anti-PD-L1 cancer immunotherapy. By promoting chromosome misalignment and missegregation in p53-deficient cancer cells with unrepaired DSBs, DNA-PK inhibitor accelerated micronuclei formation, a key generator of cytosolic DNA and activator of cGAS/STING-dependent inflammatory signaling as it elevated PD-L1 expression in irradiated cancer cells. Triple combination of radiation, peposertib, and bintrafusp alfa, a fusion protein simultaneously inhibiting the profibrotic TGFβ and immunosuppressive PD-L1 pathways was superior to dual combinations and suggested a novel approach to more efficacious radioimmunotherapy of cancer.

Implications: Selective inhibition of DNA-PK in irradiated cancer cells enhances inflammatory signaling and activity of dual TGFβ/PD-L1 targeted therapy and may offer a more efficacious combination option for the treatment of locally advanced solid tumors.

Introduction

Double-strand breaks (DSB) are the most lethal lesions in DNA and their repair has been considered an attractive intervention point for developing new or potentiating established cancer therapeutics (1–3). Non-homologous end joining (NHEJ) is the main molecular pathway for DSB repair, used 80% to 90% of the time in cancer cells (4, 5). Although error-prone, it is a quick and efficient way for restoring the integrity of the affected chromosomes and preventing the potentially detrimental consequences in actively proliferating cells (6–8). NHEJ is driven by DNA-dependent protein kinase (DNA-PK) in association with several other molecular components, Ku70, Ku80, XRCC4, ligase IV, and artemis, assuring proper resection and resealing of the broken DNA strands in a timely manner (8–10). DNA-PK kinase activity is critical for the execution of its important DNA repair function (11) and several small-molecule inhibitors have been reported to suppress NHEJ repair and potentiate ionizing radiation (IR) and DSB-inducing chemotherapy (2, 12).

Peposertib (M3814) is a potent and selective DNA-PK inhibitor with optimized pharmacologic properties currently in early clinical development in combination with radiotherapy (13, 14). It effectively suppresses the repair of DSBs induced by IR or chemotherapeutic agents, strongly enhances cancer cell killing and improves therapy outcome in preclinical tumor models of radiotherapy (13). In cancer cells expressing wild-type p53, M3814 boosts ATM/p53 signaling and reinforces p53-mediated cell-cycle checkpoint control, leading to premature senescence of irradiated cancer cells. This overactivation of the natural p53 response effectively protects p53 wild-type cancer cells from the lethal consequences of proliferation with persistent DSBs. However, in the absence of functional p53 this protective mechanism is lost, and cancer cells enter into replication and mitosis with unrepaired DSBs, resulting in aberrant division and ultimately cell death (15).

It is well established that inhibition of NHEJ by targeting DNA-PK potentiates the antitumor activity of DSB-inducing agents, including radiation (13), but the mechanisms driving these effects have not been well characterized (2, 3). Using M3814 as a selective molecular tool, we investigated the main cellular events leading to enhanced killing of irradiated p53-deficient cancer cells. Our data reveal that cancer cells cycling with persistent DNA DSB damage, promoted by M3814, suffer severe chromosome abnormalities, misalignment, missegregation, and intense micronucleation leading to strong activation of cGAS/STING-mediated inflammatory response. These findings combined with the elevated expression of PD-L1 protein in irradiated cancer cells provided a clear rationale for combination with PD-1 checkpoint targeted immunotherapy. Triple combination of M3814, IR and bintrafusp alfa (BA, M7824), a bifunctional fusion protein targeting TGFβ and

[1]Translational Innovation Platform Oncology and Immuno-Oncology, EMD Serono Research & Development Institute, Inc., Billerica, Massachusetts. [2]Translational Innovation Platform Oncology and Immuno-Oncology, Merck KGaA, Darmstadt, Germany.

Note: Supplementary data for this article are available at Molecular Cancer Research Online (http://mcr.aacrjournals.org/).

M.I. Carr, L.-Y. Chiu, and Y. Guo contributed equally to this article.

Corresponding Author: Lyubomir T. Vassilev, Translational Innovation Platform Oncology and Immuno-Oncology, EMD Serono Research & Development Institute, Inc., 45A Middlesex Turnpike, Billerica, MA 01821. Phone: 978-294-1115; E-mail: lubo.vassilev@emdserono.com

Mol Cancer Res 2022;20:568–82

doi: 10.1158/1541-7786.MCR-21-0612

PD-L1, demonstrated superior efficacy and survival benefit in three syngeneic murine tumor models. Our results revealed that selective DNA-PK inhibition by M3814 not only effectively enhances cancer cell killing but also provides a powerful mechanism for induction of inflammatory micronucleation thus offering a new combination approach to more efficacious radioimmunotherapy of cancer.

Materials and Methods

Reagents and cell culture

Peposertib was synthesized at Merck KGaA. Bintrafusp alfa and the isotype control were manufactured by EMD Serono, Inc. MRT67307 was obtained from MilliporeSigma. RO3306 and nocodazole were purchased from SelleckChem. ON-TARGETplus Non-targeting siRNA Control pool (D-001810-10-05) and ON-TARGETplus Human TMEM173 siRNA pool (L-024333-00-0005) were purchased from Dharmacon. Human and murine cell lines were obtained from ATCC if not indicated otherwise. Cell line identity was confirmed by short tandem repeat analyses and *Mycoplasma* infection was excluded by PCR-based testing. HeLa, A549, MC38, and B16F10 cells were cultured in DMEM and H1299 and 4T1 cells were cultured in RPMI1640 media. All media were supplemented with 10% heat-inactivated FCS (Corning). HeLa NucLight cells were cultured according to the manufacturer's recommendations. A549 p53-null cell clone was generated by CRISPR as described previously (15). HeLa-GFP-H2B cells (16) were provided by Geoffrey Wahl, Salk Institute for Biological Studies (San Diego, CA). The MC38 murine colon carcinoma cell line was a gift from the Scripps Research Institute. siRNA transfections were performed using Lipofectamine RNAiMax (Invitrogen) according to the manufacturer's instructions.

Gene expression analysis

RNA was isolated by RNeasy Mini Kit with on column DNase digestion (Qiagen). RNA purity and concentration were determined using a Nanodrop spectrophotometer (Thermo Fisher Scientific). For NanoString analysis, RNA samples (50 ng) were hybridized using the nCounter Human v1.1 PanCancer Immune Panel (NanoString) in accordance with the manufacturer's protocol. For quantitative PCR analysis, cDNA was synthesized using Superscript IV VILO Master Mix (Thermo Fisher Scientific) as described by manufacturer. qPCR was performed (on 10–100 ng input cDNA) using TaqMan Fast Advanced Master Mix and a QuantStudio 7 Flex Real-Time PCR instrument (Applied Biosystems). TaqMan probes used are listed in the Supplementary Materials and Methods. Relative fold-change ($\Delta\Delta C_t$) gene expression was normalized to GAPDH.

Western blots and MSD assays

Cells were lysed in RIPA buffer (Cell Signaling Technology, #9806) supplemented with protease and phosphatase inhibitors (Roche Diagnostics), as described in manufacturer's protocol. Protein concentration of extracts was quantified by the BCA assay (Pierce, #23227). Western samples were prepared using NuPAGE LDS sample buffer and reducing Agent. Samples were resolved on NuPAGE 4% to 12% Bis-Tris Midi Gels and transferred to nitrocellulose membranes via iBlot Dry Blotting System (Thermo Fisher Scientific). Membranes were treated and imaged with a LI-COR Odyssey CLx imaging system in accordance with the LI-COR Near-Infrared Western Blot Detection Protocol (LI-COR). Antibodies used are listed in the Supplementary Materials and Methods. Cytokine/chemokine concentration in media was determined by sandwich immunoassay using U-Plex Assays and a Sector Imager 1300 (Meso Scale Discovery, MSD) in accordance with the manufacturer's protocol. Protein concentrations were normalized to RNA content for each treatment condition and calculated as fold change compared with DMSO controls.

Cell-cycle analysis

Cells were harvested and fixed in cold 70% ethanol overnight at 4°C prior to staining with Propidium iodide/RNase Staining buffer (BD Biosciences, 550825) for 15 minutes at room temperature. For two-dimensional analysis, FITC BrdU Flow Kit (BD Biosciences, 559619) was used as described previously (15). Cell-cycle profiles were analyzed using a BD FACS Canto flow cytometer (BD Biosciences) and data were processed with FlowJo software.

IncuCyte live-cell imaging and analysis

HeLa NucLight cells (Essen BioScience, 4490) were seeded in 96-well plates and incubated overnight at 37°C and 5% CO_2. The next day, cells were treated with M3814 for 1 hour followed by IR (5 Gy). IncuCyte Cytotox red reagent (Essen BioScience, 4632) was added to the medium to label dead cells in real time. Images were taken every 2 hours using an IncuCyte ZOOM (Essen BioScience). Cell growth curve was quantified by counting the number of fluorescent green nuclei. Relative cell death is determined by the number of IncuCyte Cytotox red counts normalized to total number of green counts per well. To track individual cell undergoing mitosis, HeLa NucLight and HeLa GFP-H2B cells were treated as indicated, cells were imaged at 10 minutes intervals using the 20× objective for 7 days. Analysis was carried out using ImageJ software (NIH, Bethesda, MD).

Metaphase spreads and spectral karyotyping analysis

Cells were plated in T75 flasks overnight and pretreated with M3814 (1 μmol/L) for 1 hour before IR (5 Gy). After 48 hours, 150 nmol/L nocodazole was added and the cells were incubated for additional 18 hours. Metaphase cells were collected by shake-off and exposed to a hypotonic buffer (0.57% KCl) at 37°C for 30 minutes. Cells were fixed with fresh ice-cold methanol:acetic acid (3:1), dropped onto slides, stained with Giemsa, and >60 metaphase spreads/condition were scored for chromosomal aberrations. For spectral karyotyping, fixed cells were processed and analyzed at the Molecular Cytogenetic Core, Albert Einstein College of Medicine, Bronx, NY as described previously (17). Ten randomly picked metaphase spreads were imaged/analyzed for each treatment condition.

Immunofluorescence assay

A total of 6×10^4 cells/well were seeded in 6-well plates on day 0, and preincubated in 1 μmol/L M3814 or DMSO 1 hour before IR (5 Gy). Cells were fixed with methanol and blocked with MAXblock (Active Motif, 15252) for 1 hour. Samples were incubated with primary antibodies for 1 hour, washed and incubated with secondary antibodies and DAPI (Invitrogen, D1306) for 1 hour. Coverslips were then mounted with ProLong Gold Antifade Mountant (Invitrogen, P36934). Image acquisition and analysis were performed with Zeiss MIC-074. Antibodies used are listed in the Supplementary Materials and Methods.

Murine tumor model studies

C57BL/6 and BALB/c mice were obtained from The Jackson Laboratory and Charles River Laboratories, respectively. All mice used for experiments were 6 to 12 week old females. Mice were housed with ad libitum access to food and water in pathogen-free facilities. Detailed protocols of tumor studies and CD8 IHC are described in the Supplementary Materials and Methods.

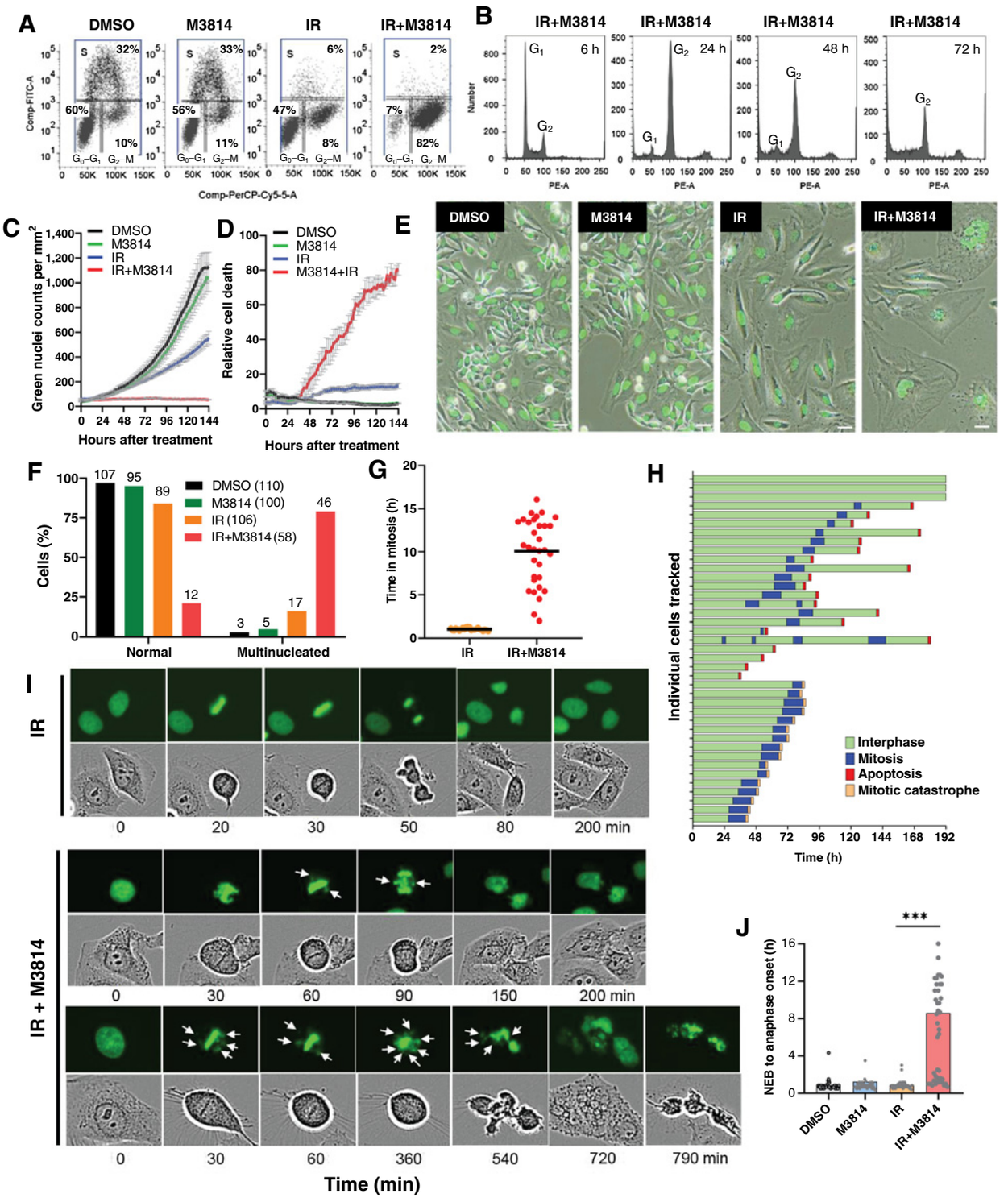

Figure 1.

Exposure of irradiated p53 dysfunctional cells to M3814 leads to misalignment and missegregation of multiple chromosome and enhanced cell death. **A,** Cell-cycle distribution of HeLa cells exposed to vehicle (DMSO), M3814 (1 μmol/L), IR (5 Gy), or IR (5 Gy)+ M3814 (1 μmol/L) for 24 hours. Cells were incubated with bromodeoxyuridine (BrdU) for 1, harvested and stained with anti-BrdU antibody and 7-AAD for flow cytometry. The percentage of cells in each cell-cycle phase was calculated and rounded to the next digit. **B,** Cell-cycle distribution profiles of HeLa cells exposed to IR (5 Gy)+M3814 (1 μmol/L) for 6, 24, 48, and 72 hours. Cells were collected, stained with propidium iodide, and analyzed by flow cytometry. Growth curves (**C**) and relative cell death (**D**) of HeLa NucLight cell exposed to vehicle, M3814, IR, or IR+M3814. Cells were treated as in **A** in the presence of Cytotox red reagent and imaged every 2 hours for 6 days by IncuCyte with a 10× objective. Cell growth was plotted as the number of green fluorescent nuclei for each timepoint. Relative cell death was determined by normalizing the Cytotox red counts to green nuclei counts and shown as mean ± SD. (*Continued on the following page.*)

Statistical analyses

All statistical analyses were performed using GraphPad Prism Software, version 7.0. Experimental data were analyzed with Student *t* test unless indicated otherwise. Tumor volume data are presented graphically as mean ± SEM by symbols or as individual mice by lines. Other statistical methods are described in the figure legends. Statistically significant differences are labeled with *, $P < 0.05$; **, $P < 0.01$; ***, $P < 0.001$; ****, $P < 0.0001$.

Results

M3814 augments radiation-induced cancer cell killing by amplifying aberrant mitoses.

We have shown that M3814 dramatically enhances the killing of irradiated HeLa NucLight cells (15), in which p53 is functionally disabled by HPV16-encoded E6 oncoprotein (18). This cellular model expresses GFP in the nuclear lamina, allowing improved live imaging and analysis of changes in nuclear and cellular morphology. In the following experiments, HeLa NucLight and other cancer cells were exposed to IR (5 Gy) and M3814 (1 μmol/L) previously shown to inhibit DNA-PK activity over 80% in multiple cell lines (13, 15). We first examined the effects of radiation, M3814, and the combination thereof on cell-cycle progression in proliferating HeLa cells 24 hours posttreatment (**Fig. 1A**). M3814 alone had an insignificant effect on cell-cycle distribution and growth. IR partially arrested cells in G_1–S and G_2–M phase, while the combination of IR+M3814 shifted the arrest to predominantly G_2–M. The reduced mitotic cell count indicated that the arrest is in G_2-phase (15). The G_2 arrest is likely due to elevated CHK1 and CHK2 activity resulting from increased DSB damage in the presence of M3814 (15). However, the arrest was transient and within the next 24 hours cells entered mitosis in the presence of M3814 (Supplementary Fig. S1A video). At 72 hours, the cell-cycle profile indicated a substantial increase of cell populations undergoing apoptosis (sub-G_1) or polyploidy (>4n; **Fig. 1B**). Live imaging of cell growth confirmed that the effect of M3814 was practically indistinguishable from the control (**Fig. 1C**). Radiation alone only partially affected cell growth/viability (**Fig. 1C**) while IR+M3814 was very effective at restricting HeLa cell growth (**Fig. 1C**) and produced a significant fraction of dead cells which progressively increased over 6 days (**Fig. 1D**). Only a slight increase in relative cell death was induced by IR alone. These results indicated that M3814 is a potent cell death enhancer in irradiated HeLa cells.

Live-cell imaging for 6 days (**Fig. 1E**) showed that 17% of the cells exposed to IR alone had multiple/fragmented nuclear morphology (**Fig. 1E** and **F**). This fraction increased to 78% in response to IR+M3814 treatment (**Fig. 1F**). The small fraction of surviving cells at was predominantly multinucleated and exhibited a typical senescence-like morphology (**Fig. 1E**; Supplementary Fig. S1A). Time-lapse videos (Supplementary Fig. S1A) revealed that most of the cells had undergone abnormal mitoses with substantially prolonged duration, frequent tripolar spindles, cytokinesis failure, polyploidy, and recurrent cell death either in mitosis or interphase (Supplementary Fig. S1B and S1C). The length of mitosis increased from 1.5 hours in the IR-only cells to 10 hours in the IR+M3814-treated cells suggesting engagement of the spindle checkpoint and/or defects in chromosome attachment and segregation (**Fig. 1G**). Detailed analyses of cell morphology indicated two primary cell fates in IR+M3814-treated cells (**Fig. 1H**). Nearly half of the tracked cells (16/39) died in mitosis and 16/39 cells underwent mitotic arrest, followed by slippage and died in interphase (Supplementary Fig. S1B and S1C-video). A relatively small fraction (4/39) died without entering mitosis and 3/39 cells remained alive without entering mitosis and developed a senescence-like phenotype. Although heterogeneous in nature, the treatment outcome in the population of HeLa cells exposed to IR+M3814 suggested that most cells suffered from an inability to perform normal mitotic division.

We next examined chromosome behavior during mitosis. For this purpose, we used a HeLa cell model with histone H2B fused GFP, allowing live imaging of chromosomes and their movement during mitosis (16). HeLa-GFP-H2B cells were exposed to IR or IR+M3814 treatment and time-lapse videos were recorded (Supplementary Fig. S2A). Analysis showed that most cells exposed to vehicle or M3814 underwent normal mitoses, with all chromosomes aligned at the metaphase plate and normal chromosome separation at anaphase (DMSO: $n = 50/50$, M3814: $n = 48/50$). The majority of examined mitoses in cells exposed to IR alone were also normal (**Fig. 1I**; Supplementary Fig. S2A) though 27% ($n = 14/52$) exhibited some degree of chromosome misalignment and missegregation. The limited fraction of affected cells with high degree of aberrations in the IR-treated samples allowed the bulk of the cell population to continue proliferating over the 7-day period (Supplementary Fig. S2B). IR+M3814 treatment led to prolonged mitoses in most cells and multiple chromosome misalignment/missegregation events in 88% ($n = 44/50$) of the examined mitoses (**Fig. 1I** and **J**; Supplementary Fig. S2C). The average time from nuclear envelope breakdown to anaphase in the tracked cells exposed to IR+M3814 was 8 hours, compared with approximately 1 hour for all other conditions (**Fig. 1J**), indicating severe problems in chromosome attachment and/or segregation. Time-lapse imaging detected multiple examples of chromosomes unable to attach to the spindle (**Fig. 1I**; Supplementary Fig. S2C). Because of the smaller fraction of cells with chromosome alignment/segregation defects, IR-exposed samples showed increased proportions of seemingly normal cells in the population over the course of the experiment. The balance of cell growth/death was dramatically shifted in the IR+M3814-treated samples, where the bulk of the initial cell population underwent cell death, leaving a small fraction of surviving cells with a senescence-like phenotype and aberrant (multinucleated/fragmented) nuclear structure (**Fig. 1E**). These results revealed that impaired chromosome attachment, alignment, and/or segregation at the mitotic spindle are the main mechanism behind M3814-enhanced death in irradiated HeLa cells.

(*Continued.*) **E,** Representative still images from **C** at day 6. Scale bar: 20 μmol/L. **F,** Percentage of multinucleated cells (>2 nuclei/cell) was determined from live-imaging videos of HeLa NuclLight cells treated as in **C**. **G,** Time in mitosis of HeLa NucLight cells treated with IR (5 Gy) or IR (5 Gy)+M3814 (1 μmol/L) and continuously imaged by IncuCyte with a 20× objective. Individual cells exposed to IR ($n = 20$) or IR+M3814 ($n = 39$) were tracked and analyzed. Bars indicate population averages. **H,** Cell fate in response to combined IR (5 Gy)+M3814 (1 μmol/L) treatment. HeLa NucLight cells from **G** were tracked to determine their fate in relation to mitosis within 192 hours after exposure to IR (5 Gy) + M3814 (1 μmol/L). Time spent in interphase (green bars) and mitosis (blue bars). Truncated bars indicate onset of cell death in interphase (red) and in mitosis (orange). **I,** Representative images of mitotic progression of HeLa GFP-H2B exposed to IR (5 Gy) or IR (5 Gy)+M3814 (1 μmol/L). HeLa GFP-H2B cells were treated as in **E** and imaged by IncuCyte with a 20× objective. Individual cells were tracked and analyzed. Representative GFP and phase contrast images and the time from start of cell tracking are shown. Arrows point to examples of misaligned and/or lagging chromosomes. **J,** The lengths of time from nuclear envelop breakdown (NEB) to anaphase onset in HeLa GFP-H2B determined as in **G**.

M3814 hinders IR-induced DSB repair and causes severe chromosome abnormalities

Chromosome misalignment and mis-segregation during mitosis have been shown to correlate with structural chromosomal aberrations (19–21). We therefore examined the effect of M3814 on metaphase chromosomal morphology in irradiated cells. For this purpose, we chose a p53-null clone of the widely used A549 cellular model (A549p53KO), that was previously generated by CRISPR knockout (KO) to assess the role of p53 in response to M3814 (15). A549 cells express wild-type p53 and undergo complete cell-cycle arrest and premature senescence when irradiated in the presence of M3814. Deletion of p53 removes this protective barrier and allowed to examine the consequences of cycling with DSBs (15).

A549p53KO cells were exposed to IR and/or M3814 for 48 hours followed by nocodazole for an additional 18 hours to enrich in metaphase cells. Metaphase chromosome spreads were prepared, and chromosome morphology examined. Relatively few visible chromosome abnormalities could be seen in the vehicle or M3814 treated cells (**Fig. 2A**). The fraction of cells with chromosome aberrations increased significantly in the irradiated cells but was dramatically higher in the cells undergoing the combination treatment where examples of chromosome fusion (a), ring (b), breaks/loss (c, d) were identified, frequently together with many chromosome fragments (**Fig. 2A**, arrows). Quantitative analyses of the images from at least 60 metaphase spreads indicated that vehicle and M3814-treated controls have a small percentage of aberrations (<5%) and no chromosome fragmentation (**Fig. 2B**). The fraction of metaphase spreads with aberrant chromosomes increased to 20% (including 7% fragmented) in the irradiated cells. In response to the combination treatment, approximately 75% of the spreads exhibited aberrant chromosome morphology, of which 38% were fragmented (**Fig. 2B**).

To better understand the type and magnitude of chromosomal damage, cells treated as above were subjected to spectral karyotyping analyses. Ten randomly selected metaphase spreads from each treatment were stained with chromosome-specific probes and their karyotypes examined (**Fig. 2C**; Supplementary Figs. S3 and S4). The analyses indicated that IR+M3814 treatment caused a marked increase in chromosomal abnormalities compared with radiation alone. Both the average number of chromosomes and/or fragments (**Fig. 2D**) and overall number of abnormal chromosomes (**Fig. 2E**) were substantially higher. The most dramatic difference was in the number of unidentifiable chromosome fragments known as markers (19, 22), which were present only in IR+M3814-treated samples (**Fig. 2F**). These findings indicated that by inhibiting the repair of IR-induced DSBs, M3814 promoted severe structural abnormalities and chromosome fragmentation.

M3814-enhanced chromosome damage give rise to intense micronucleation in irradiated cancer cells

Chromosome analysis in the p53-null A549 cells revealed that by extending the life of IR-induced DSBs M3814 can amplify the effect of radiation resulting in structural changes in most metaphase chromosomes. These changes, especially the high degree of fragmentation, could adversely affect the ability of chromosomes to properly attach to the mitotic spindle and segregate during anaphase. As a result, lagging chromosomes may form that remain outside of the newly assembled daughter nuclei as independent micronuclei (MN; ref. 23). We investigated these events using the A549p53KO cells. As shown previously (15), A549 cells are completely arrested in G_1 and G_2 phases and acquired premature senescence. The p53-null cells underwent partial and transient G_2 arrest allowing a substantial cell fraction to replicate and divide with unrepaired DSBs and ultimately die from the consequences (15). A549p53KO cells exposed to IR plus/minus M3814 were enriched in mitotic cells with the help of the CDK1 inhibitor RO-3306 (24) and examined by immunofluorescent microscopy (**Fig. 3A**). The bulk of cells exposed to IR formed relatively normal mitotic figures; however, multiple IR+M3814-treated cells were captured undergoing aberrant mitosis. Examples of a cell in metaphase with grossly misaligned chromosomes and multiple γH2AX foci and a cell captured in anaphase with several lagging chromosomes were shown (**Fig. 3A**).

We next looked for the presence of MN. No identifiable MN were found in the A549 cells under combined treatment (**Fig. 3B** and **C**). A549p53KO cells had at least one MN in 4% of IR-exposed cells but 72% in the cells under IR+M3814 treatment (**Fig. 3B** and **C**). A high MN number was also observed in response to IR+M3814 in the p53KO line of another isogenic cell line cell pair, HT1080 (Supplementary Fig. S5A and S5B; ref. 15). Immunofluorescent staining of the A549 cell lines at day 7 under IR+M3814 showed single nuclei in the senescent A549p53WT cells with multiple γH2AX foci contained in the nuclear structure (**Fig. 3D**; Supplementary Fig. S5B). A549p53KO cells exhibited multiple MN with strong staining for γH2AX (**Fig. 3D**), indicating that MN are formed predominantly around heavily damaged chromosomes or chromosomal fragments (**Fig. 3A**). Similar results were obtained in the HT1080 cell line pair after IR+M3814 at day 7 (Supplementary Fig. S5C). Seven days after radiation, A549p53KO cells showed sporadic MN, with 1 MN in 10% (2/20) and 2 MN in 20% (4/20) of examined cells (**Fig. 3E**). In contrast, the combined treatment induced numerous MN (3 to18 per cell, average 8) in all examined cells (23/23; **Fig. 3E**).

Chromosomes that cannot properly attach and segregate during mitosis are spontaneously enveloped by nuclear lamina, which is frequently deficient in lamin B1, a marker for structural membrane integrity (25). We assessed the nuclear morphology and status of lamin B1 in the A549p53WT/A549p53KO cell lines at day 7 after IR+M3814. As described previously (15), the proliferation of A549 cells was arrested, acquired premature senescence with single, well-shaped nuclei. A549p53KO cells showed multinucleated morphology with multiple detectable MN (**Fig. 4A**). Lamin B1 staining was seen consistently in the nuclear lamina of both cell lines but no signal was detected in most micronuclei identifiable by DNA staining. We then tested a parallel set of IR+M3814-treated A549 and A549p53KO samples for cGAS protein, a sensor of cytosolic DNA, and found intense staining colocalized with DAPI-stained micronuclei (**Fig. 4B**). These experiments indicated that the nuclear lamina of many micronuclei induced by the IR+M3814 combination in A549p53KO cells were lamin B1-deficient allowing cGAS to detect cytosolic DNA. Our studies revealed that continuous exposure of p53-deficient A549 cells to DNA-PK inhibitor, suppresses the repair of IR-induced DSBs and promotes severe structural defects in chromosomes resulting in aberrant mitotic division, massive micronucleation, and cytosolic exposure of chromosomal DNA. Given the role of cGAS in triggering inflammatory responses our experiments suggested that M3814 may greatly potentiate inflammatory signaling in irradiated cancer cells.

M3814 is a powerful enhancer of radiation-induced inflammatory response in p53-deficient cancer cells

To test the effect of M3814 on inflammatory signaling, A549 and A549p53KO clones were exposed to IR, M3814, or the combination and gene expression was analyzed via NanoString nCounter PanCancer Immune Profiling Panel at days 3 and 7. Relative to IR alone, IR+M3814 treatment induced markedly greater expression of a

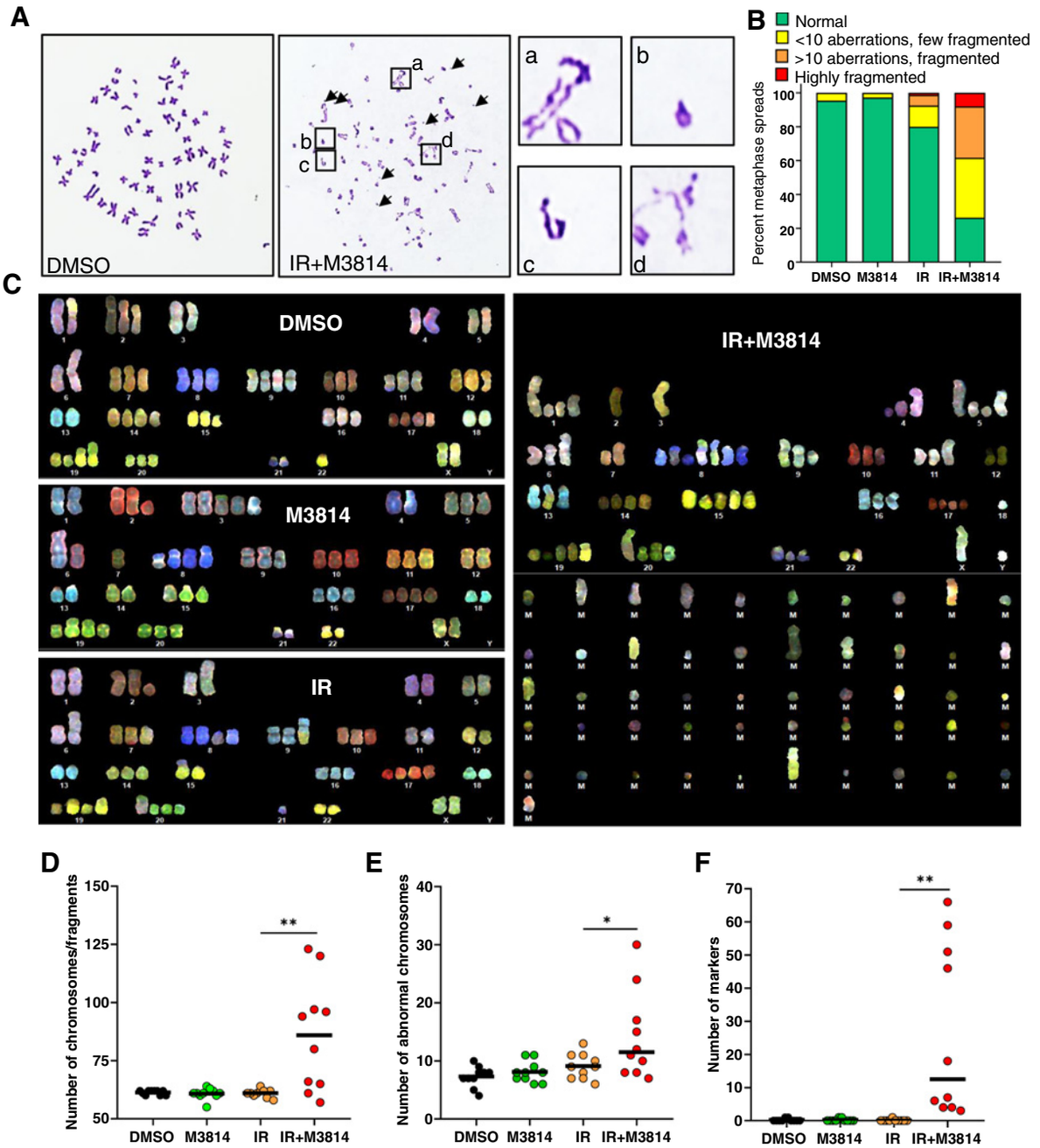

Figure 2.

M3814 promotes gross chromosomal aberrations in irradiated p53-null A549 cells. **A,** A549p53KO cells were exposed to DMSO, M3814 1 μmol/L), IR (5 Gy), or IR (5 Gy) + M3814 (1 μmol/L) for 48 hours, metaphase spreads were generated, collected, and analyzed. Shown are representative images of spreads from DMSO and IR+M3814-treated cells. Examples of chromosome aberrations, including fragmentation (arrows), fusion, ring, breaks/loss are highlighted in boxes a–d. **B,** Quantification of chromosomal aberrations and fragmentation. A549p53KO cells were treated as in **A** and metaphase spreads (>60 per condition) were analyzed. Few fragmented: spreads with <10 aberrations and fragments; Fragmented: >10 aberrations and fragments; highly fragmented: most chromosome fragmented. **C,** Spectral karyotyping images. Proliferating A549p53KO cells were treated as in **A** for 48 hours and metaphase spreads collected. Ten randomly picked metaphase spreads were karyotyped from each treatment condition. Chromosomes are numbered, M designates "Marker" chromosomes. Quantification of spectral karyotyping data is shown in **D–F**. **D,** Individual and average numbers of chromosomes/fragments per metaphase spread as described in **C**. **E,** Number of chromosomal abnormalities including deletion, duplication, translocation, and insertion per metaphase spread. **F,** Number of marker chromosomes in each metaphase spread.

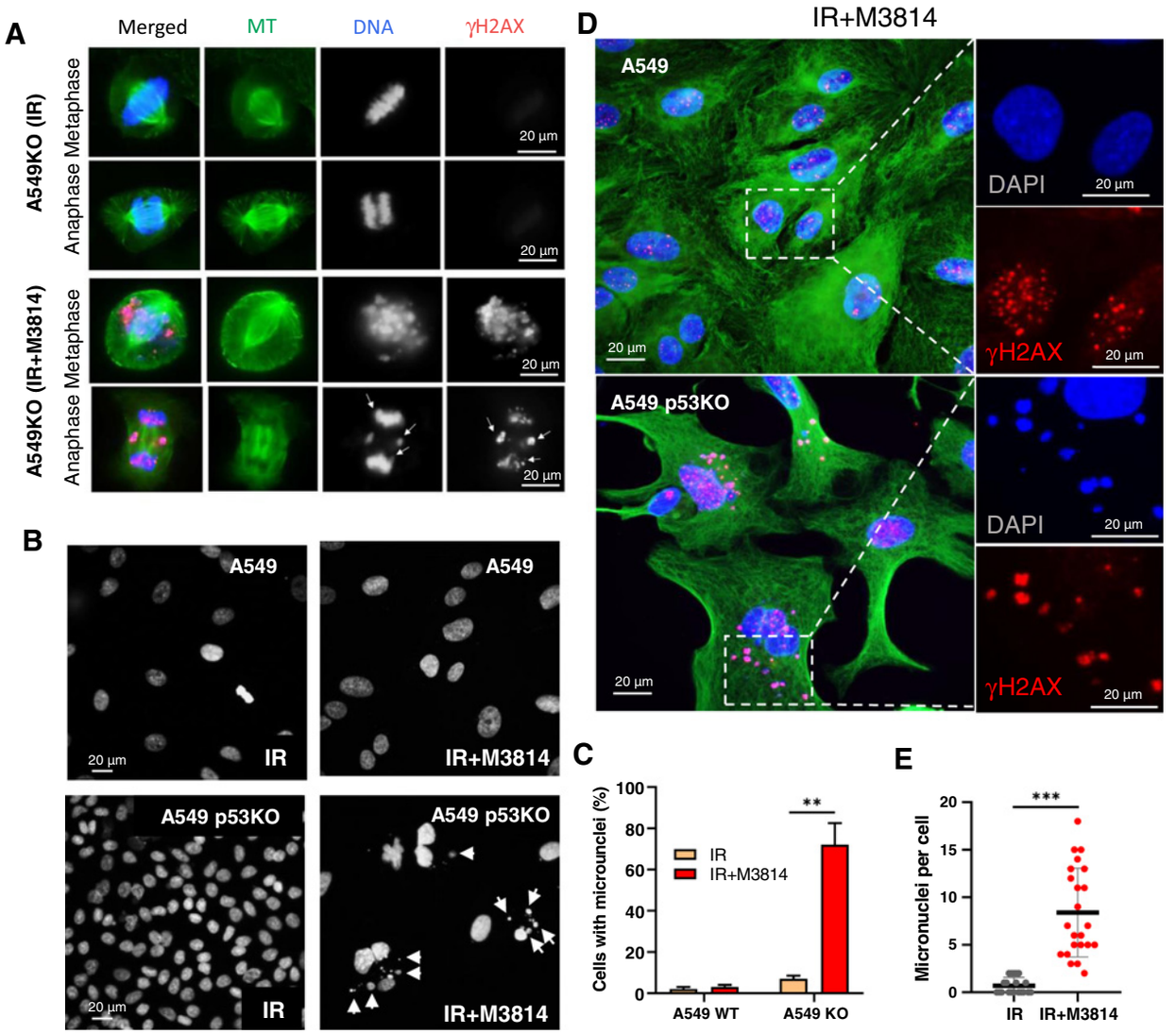

Figure 3.

M3814-induced structural defects in multiple chromosomes lead to massive micronucleation in p53-deficient cancer cells. **A,** A549p53KO cells were exposed to IR (5 Gy), or IR (5 Gy) + M3814 (1 μmol/L) for 48 hours and then to CDK1 inhibitor RO-3306 for 16 hours to arrest cells at the G_2–M border. The population was enriched in mitotic cells by release from the RO-3306 block and immune stained for α-tubulin (green), DAPI (blue), and γH2AX (red). Representative images in metaphase and anaphase shown. **B,** Representative DAPI images of A549 and A549p53KO cells following 48 hours exposure to IR (5 Gy), or IR (5 Gy) + M3814 (1 μmol/L). Arrows indicate micronuclei. **C,** Percentage of cells with at least one micronucleus. Quantitative analyses of imaging data from **B**. **D,** Representative images of fixed A549 and A549p53KO cells at day 7 after IR (5 Gy) + M3814 (1 μmol/L) treatment, stained for α-tubulin (green), DAPI (blue), and γH2AX (red). **E,** Total number of micronuclei per cell. Quantification of imaging data parallel treatment as in **D**.

multitude of immune-related genes in both cell lines (**Fig. 5A**). However, much stronger gene induction was observed in the A549p53KO cells. M3814 treatment alone had little impact on gene expression. The greater immune-related gene activation observed in A549p53KO cells relative to the parental cells supported the hypothesis that MN formation resulting from aberrant mitosis is driving the strong inflammatory gene response. Furthermore, the higher levels of gene expression observed at day 7 relative to day 3 agree with our findings regarding the kinetics of M3814-induced senescence and micronucleation in A549p53WT and A549p53KO cells. The more aberrant mitotic cycles A549p53KO cells underwent the higher number of MNi were formed. At day 7 after IR+M3814 treatment, the surviving cell population had multiple MN per cell (**Fig. 3D** and **E**).

Among the markedly upregulated genes in IR+M3814-treated A549p53KO cells were numerous IFN-stimulated genes as well as various chemokines and cytokines associated with inflammatory response (**Fig. 5A**). The expression levels of activated genes in the cells exposed to IR+M3814 at day 7 were 5 to 300-fold higher than the DMSO controls and markedly higher than the IR controls (Supplementary Fig. S6A) indicating a remarkably strong potentiation of radiation-induced inflammatory signaling in the surviving population of cells with multiple MN. The milder version of inflammatory gene response in A549p53WT cells is indicative of gradual

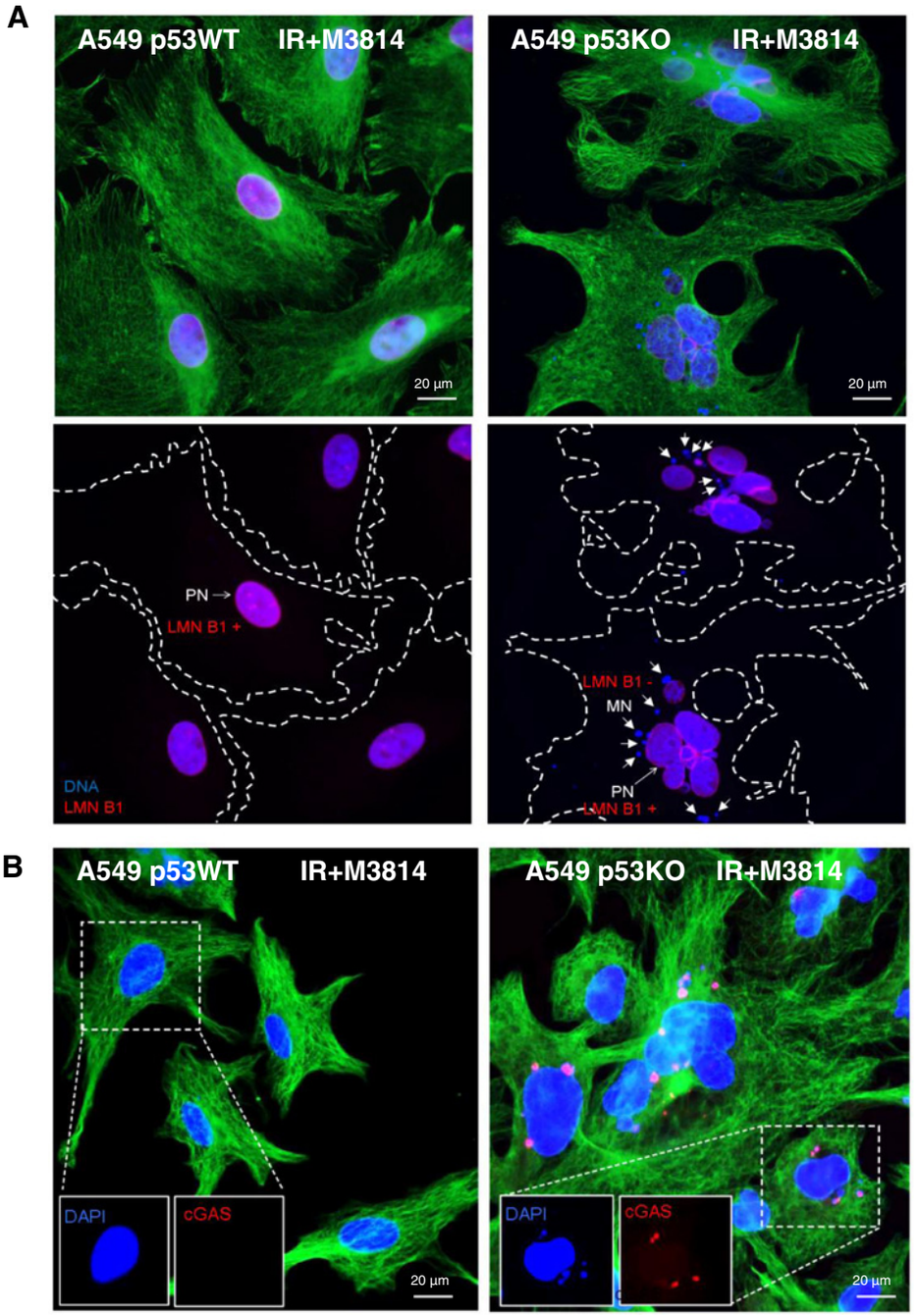

Figure 4.

M3814-induced micronuclei have compromised lamina and stain for cGAS. **A,** A549 and A549p53KO cells were exposed to IR (5 Gy) + M3814 (1 μmol/L) for 7 days. Representative image of cells stained for lamin B1 (red), DNA(DAPI, blue) and α-tubulin (green) are shown. Arrows indicate micronuclei. PN, primary nucleus. **B,** A549 p53WT and p53KO cells were treated as in **A**. Representative image of cells stained for cGAS (red), DNA (DAPI, blue), and α-tubulin (green) are shown. Magnified images were indicated in the bottom.

acquisition of senescence and senescence-associated secretory phenotype (SASP) induced by exposure to IR+M3814 (15).

IFN-stimulated genes were well represented in the set of activated genes, supporting the hypothesis that cGAS/STING signaling is a major player in the response to M3814 in irradiated A549p53KO cells. Knockdown of STING expression by siRNA substantially reduced the IR+M3814-induced expression of a subset of IFN-stimulated genes and cytokines (**Fig. 5B**). Similarly, inhibition of the downstream STING pathway mediator TANK-binding kinase 1 (TBK1), effectively prevented their activation, confirming that M3814 activated STING signaling in irradiated A549p53KO cells (**Fig. 5C**).

The changes in the protein levels of STING and several key members of its downstream pathway components in the isogenic A549 cell pair exposed to IR+M3814 at day 7 were analyzed by Western blotting (**Fig. 5D**). Phospho-TBK1, phospho-STING, and phospho-IRF3 levels were substantially elevated in agreement with the activation of the cGAS/STING signaling. Upregulation of phospho-RELA and down-regulation of its negative regulator IkB kinase indicated engagement of NFκB in the response to M3814 treatment in irradiated A549p53-null cells. Similar but much less pronounced changes were observed in the p53 wild-type cells which were arrested and exhibited a fully developed premature senescence phenotype at day 7 in the combined IR+M3814

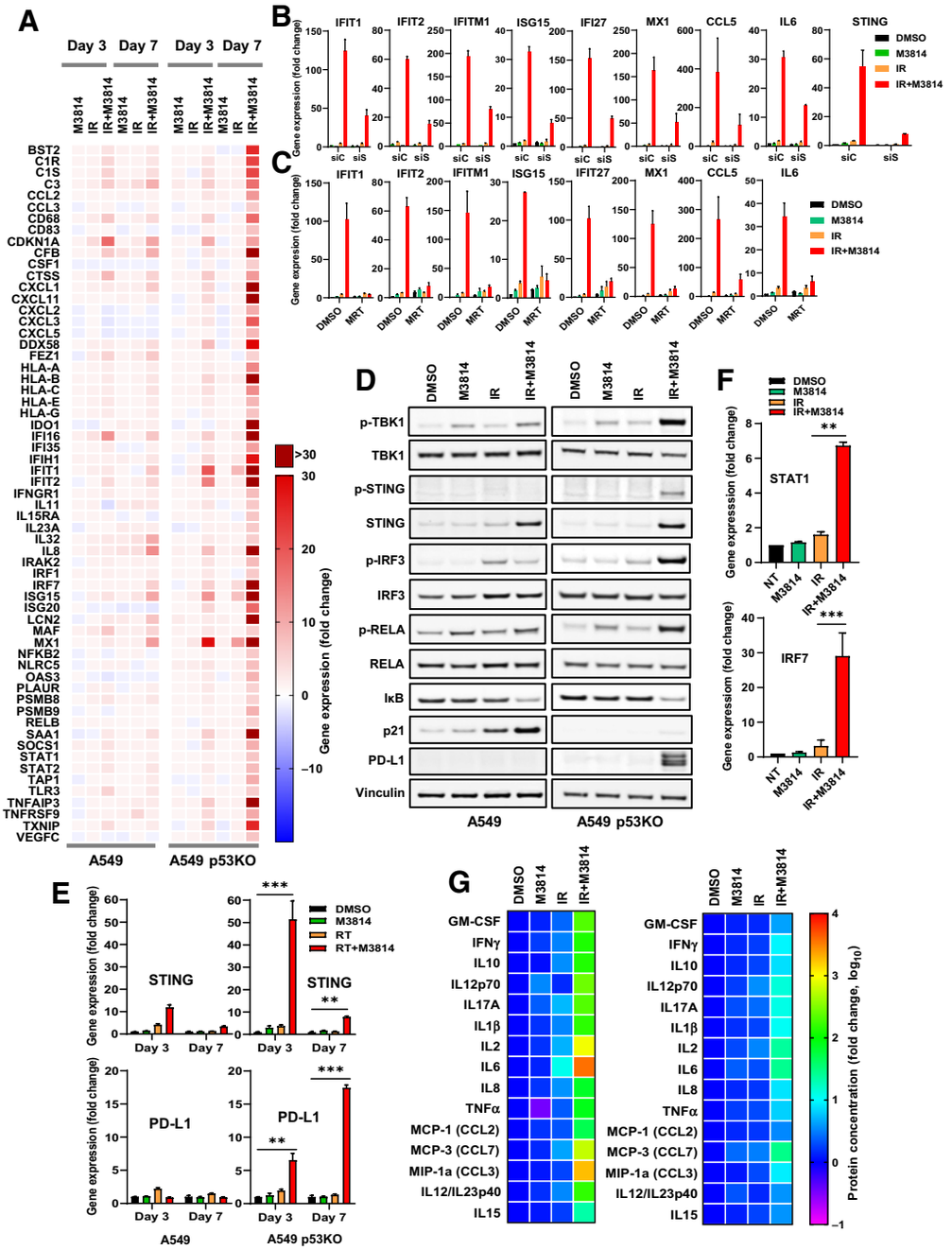

Figure 5.

M3814 enhances IR-induced inflammatory response in irradiated cancer cells. **A,** Heatmap of gene expression measured by NanoString the PanCancer Immune Panel in A549 and A549p53KO cells following 3- or 7-day exposure to DMSO, M3814, IR (5 Gy), or IR (5 Gy) + M3814 (1 μmol/L). Results were filtered to exclude genes in which sample counts were below a background threshold of 10, and to include all genes in which IR+M3814 treatment induced expression >5-fold than DMSO control in A549p53KO cells at day 7. The expression levels of the resultant 61 genes are shown as fold change. **B,** Fold change in transcript levels of IFN-stimulated and inflammatory genes as detected by qPCR. A549p53KO cells were transfected with nontargeting (siC) or TMEM173 (STING) siRNA (siS) for 24 hours and then incubated with DMSO, M3814, IR (5 Gy), or IR (5 Gy) + M3814 (1 μmol/L) for 3 days. **C,** Change in transcription levels of IFN-stimulated and inflammatory genes. A549p53KO cells were treated as in **B** with or without TBK1 inhibitor MRT67307 (3 μmol/L) for 3 days. **D,** Western blot analysis of the STING-TBK1 pathway in lysates from A549 and A549p53KO cells treated as in **C** on day 6. **E,** Fold change in transcript levels of TMEM173 (STING) and CD274 (PD-L1) measured by qPCR in A549 and A549p53KO cells after 3- and 7-day treatment as in **A**. **F,** Expression levels of STAT1 and IRF7 in A549p53KO cells following 7-day treatment as in **A**. Shown are average fold change values relative to DMSO treatment control, extracted from three independent NanoString expression panel experiments. **G,** Heatmaps depicting the relative levels of secreted cytokines detected by the MSD assay in the media of A549p53KO cells exposed to IR (5 Gy), or IR (5 Gy) + M3814 (1 μmol/L) for 7 days (left) and an additional 7 days following media removal and replating (right) shown as $\log_{10}$ ratio.

treatment (15). These changes result from senescence-induced inflammatory response to cytosolic DNA also dependent on activation of the STING/NFκB signaling (26). High levels of p21, a transcriptional target of p53, responsible for the complete cell-cycle arrest in the p53 wild-type A549 cells exposed to IR+M3814 (27) was seen only in A549 but absent in the p53-null clone, as expected.

Although the activity of STING is primarily regulated at a post-translational level where TBK1-mediated phosphorylation plays an important role, our Western analyses revealed a strong upregulation of the total STING protein, suggesting that additional circuits of regulation might be involved. STING gene expression was elevated over 50-fold at day 3 in IR+M3814-treated A549 p53KO cells but approximately 10-fold in the p53 wild-type cells. STAT1 and IRF7 were also found significantly elevated by IR+M3814 exposure at day 7 (**Fig. 5F**), consistent with the reported secondary activation loop in which STAT1 can activate STING gene transcription (28).

The Western analyses showed a strong upregulation of PD-L1 protein levels in the A549p53KO cells surviving the combined IR+M3814 treatment (**Fig. 5D**). Under the same treatment conditions, PD-L1 gene expression was found highly elevated on day 7 and moderately on day 3 in the p53-null cells (**Fig. 5E**). PD-L1 upregulation correlated with the IR+M3814 induced STING expression and activation, pointing to the recently established regulatory loop between STING and PD-L1 (29) as the likely mechanism behind the M3814-induced PD-L1 accumulation. STING signaling was effectively activated in two additional p53 dysfunctional cell lines, HeLa and H1299, albeit at variable levels (Supplementary Fig. S6B), suggesting that M3814 could serve as a universal enhancer of STING signaling in irradiated epithelial cancer cells lacking functional p53.

Inflammatory signaling includes a plethora of secreted proteins that function in a paracrine fashion to regulate the immune response. We looked at the levels of a set of 15 secreted proteins associated with inflammatory responses. Proliferating A549p53KO cells were exposed to IR plus/minus M3814 and protein concentrations were measured in the culture media at day 7 (**Fig. 5G**, left). Protein levels were largely unchanged by the M3814 alone. IR treatment significantly elevated the concentration of most proteins. The IR+M3814 combination showed a substantial increase over IR-induced levels in practically all tested proteins. Cells were replated following media removal at day 7 and cultured for an additional 7 days in drug-free media and protein concentrations were measured again as above (**Fig. 5G**, right). Though at reduced concentrations, a similar pattern was observed with significantly higher levels detected in IR+M3814-treated samples as compared with IR. These experiments indicated that the cells exposed to IR+M3814 continue to express and secrete immunomodulatory proteins. Our findings indicated that, once established, the M3814-enhanced secretory phenotype of irradiated A549p53KO cells retains the potential to affect tumor environment. Altogether, our studies demonstrated that the selective DNA-PK inhibitor peposertib is a powerful inducer of inflammatory micronucleation in irradiated cancer cells, leading to strong activation of cGAS/STING-driven inflammatory signaling with the potential to modulate the antitumor immune response. In addition, exposure of cancer cells to IR and M3814 caused a substantial upregulation of the PD-L1 immune checkpoint protein, a well-established cancer immunotherapy target (30).

M3814 enhanced the efficacy of radiation and bintrafusp alfa in three syngeneic murine cancer models

To evaluate the potential of M3814 as an enhancer of cancer immune therapy, we chose the recent addition to the anti-PD-L1 arsenal, bintrafusp alfa (31). This bifunctional fusion protein simultaneously targets the PD-L1 immune checkpoint protein and the immune-suppressive cytokine TGFβ involved in multiple tumor-promoting pathways (32), activated by IR (33) and implicated in radiation resistance (34).

We first assessed the inflammatory signaling in two p53-mutant mouse tumor cell lines, MC38 and 4T1. Gene expression levels and extracellular concentrations of a small panel of inflammatory cytokines were analyzed. As observed in the human cancer cells (**Fig. 5**; Supplementary Fig. S6), IR+M3814 induced substantially greater levels of both inflammatory cytokine mRNA and secreted proteins as compared to IR alone (**Fig. 6A**). These experiments extended the validity of our observations to mouse cells.

We previously reported enhanced antitumor activity with the combination of radiation and BA in mice bearing MC38 tumors, a highly immunogenic model (31). Therefore, we used similar scheduling scheme in which radiation was given once daily for the first 4 days. BA was given once on day 0 and M3814 was applied orally once a day for 14 days (**Fig. 6B**). In MC38 tumor-bearing C57BL/6 mice, M3814 showed no single-agent activity as expected (**Fig. 6C**). IR and BA alone slightly reduced tumor growth. M3814 enhanced the efficacy of radiation but not BA. IR+BA showed strong antitumor activity ($P < 0.0001$, day 17). However, the triple combination IR+M3814+BA resulted in superior tumor regression relative to IR+M3814 ($P < 0.0001$, day 17), or IR+BA ($P < 0.0001$, day 45). In fact, all mice treated with the triple combination had complete tumor regression over the duration of the experiment. In comparison, complete tumor regression was only observed in one other treatment group, IR+BA (56%, 5/9 mice). The triple combination extended survival to a greater degree than any other treatment (**Fig. 6D**). At the end of the experimental time course (100 days), 90% of mice in that group were still alive exceeding the median survival of IR+M3814 (27 days, $P < 0.0001$), IR+BA (77 days, $P = 0.04$), or M3814+BA (17.5 days, $P < 0.0001$).

We next examined the combination in the poorly immunogenic B16F10 model (35). BA monotherapy did not affect tumor growth in this model (**Fig. 6C**). IR alone and IR+BA slightly but significantly decreased tumor volume relative to the control ($P < 0.0001$, day 5; **Fig. 6C**). M3814 enhanced IR efficacy ($P = 0.06$, day 5). However, triple combination of IR+M3814+BA significantly further reduced tumor volume relative to IR+BA ($P < 0.0001$, day 7), or IR+M3814 ($P = 0.003$, day 9). Triple combination therapy also extended median survival (16 days) to a greater degree than the dual combination IR+M3814 (12.5 days), BA+M3814 (7 days), and BA+IR (8.5 days; **Fig. 6D**).

Finally, we evaluated the efficacy of the triple combination in Balb/C mice bearing 4T1 mammary tumors, an immune-excluded tumor model. IR or BA alone decreased tumor volume relative to isotype control ($P < 0.0001$ and $P < 0.0001$, day 10, respectively; **Fig. 6C**). Again, M3814 enhanced IR efficacy ($P < 0.0001$, day 10), confirming that M3814 is a universal booster of radiation activity. Combining IR+BA also resulted in enhanced tumor growth inhibition relative to either IR or BA alone ($P < 0.0001$, day 10). These antitumor effects were further significantly enhanced by M3814 in the triple combination relative to dual combinations M3814+BA ($P < 0.0001$, day 13), IR+BA ($P < 0.0001$, day 17), or IR+M3814 ($P < 0.0001$, day 20; **Fig. 6D**). Furthermore, M3814 increased median survival of the triple combination (28 days) relative to IR+BA (18 days), IR+M3814 (23 days), or IR alone (15 days).

To elucidate the involvement of the immune response in the efficacy of the triple combination IR+M3814+BA, we measured tumor-infiltrating $CD8^+$ T cells in 4T1 tumors 7 days after the last IR dose

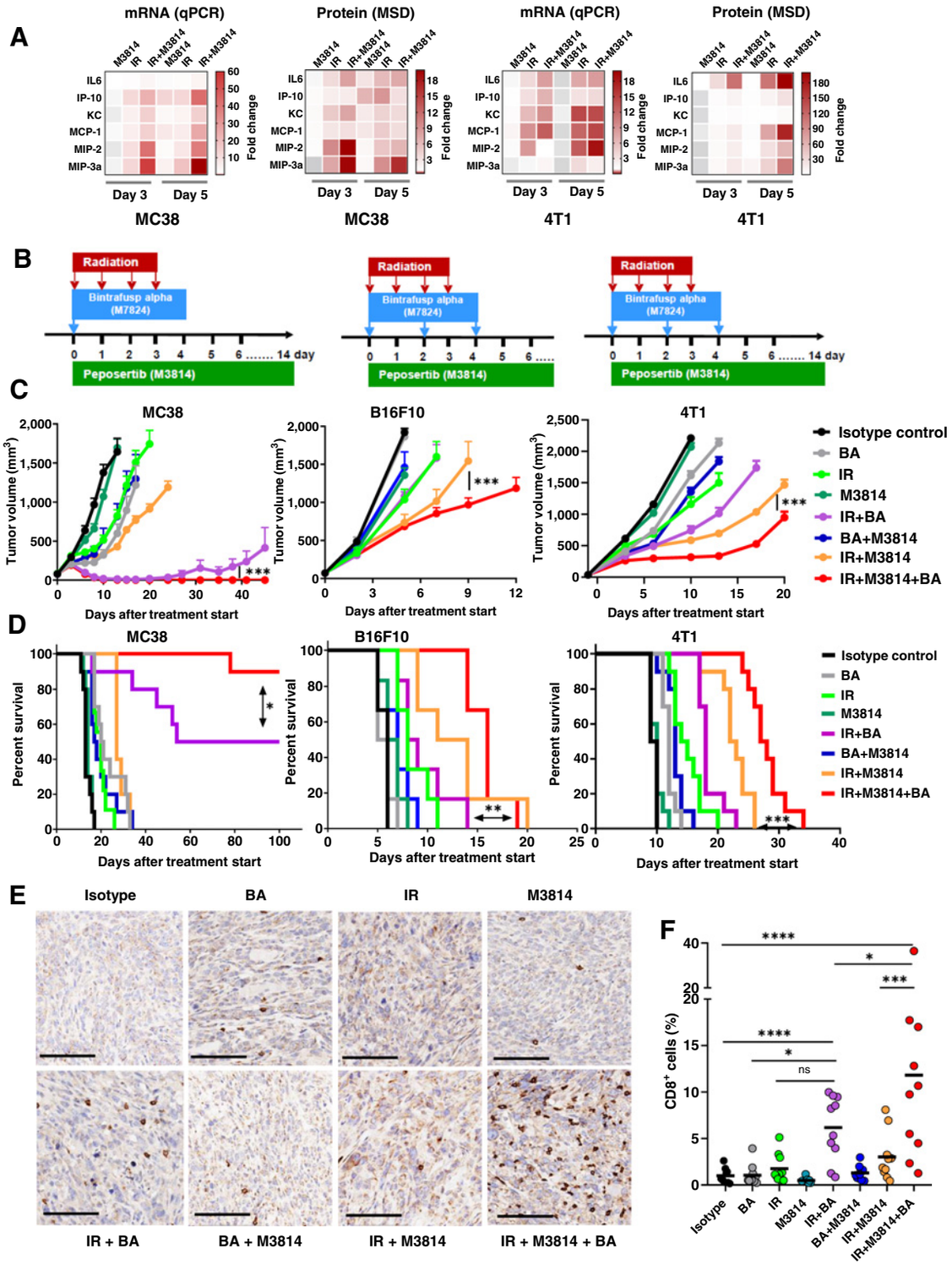

Figure 6.

Triple combination of radiation, M3814 and bintrafusp alfa shows superior efficacy and survival in syngeneic cancer models. **A,** Proliferating 4T1 and MC38 cells were exposed to IR (5 Gy) and M3814 (1 μmol/L) alone or in combination. Gene expression levels and secreted protein levels of six inflammatory signaling genes/proteins were assessed by qPCR and MSD assay, respectively. Gene expression heat maps display fold change relative to DMSO control with GAPDH as reference. Protein heatmaps display fold change relative to DMSO control, normalized to cell number (total RNA used as cell number indicator). (*Continued on the following page.*)

using IHC (**Fig. 6E** and **F**). The combination of IR+BA significantly increased the density of intratumoral $CD8^+$ cells (6.17% of nucleated cells) relative to isotype control ($P < 0.0001$), BA ($P = 0.036$), but not IR alone ($P = 0.093$). The triple combination further increased intratumoral $CD8^+$ cell density (11.8% of nucleated cells) relative to isotype control ($P < 0.0001$), IR+BA ($P = 0.017$), and IR+M3841 (3.0% of nucleated cells; $P < 0.001$; **Fig. 6F**). These data indicate that the triple combination therapy enhances the antitumor immune response over that of the respective dual combination or monotherapies.

Discussion

Radiotherapy is the mainstay of cancer therapy with nearly 60% of all patients undergoing radiation treatment during the course of their disease (36, 37). Despite continuous improvements in the delivery of radiation to the tumor, the development of effective new radiation combination therapies is still lagging (38). The antitumor activity of IR is primarily derived from the generation of DSBs in DNA, the most lethal lesions that, if left unrepaired, could induce cancer cell death by diverse mechanisms. Therefore, targeting DSB repair machinery in tumors is an emerging field in cancer therapy with several new therapeutic modalities in clinical development (3, 5). Peposertib is a potent and selective inhibitor of DNA-PK kinase activity that effectively suppresses NHEJ repair of DNA DSBs, potentiates radiation and regresses human xenograft tumors (13). In the absence of functional p53, checkpoint control in irradiated cancer cells is attenuated, cells with unrepaired DSBs enter replication and mitosis leading to mitotic catastrophe and enhanced cell death (15).

The data presented here show that most catastrophic events in irradiated cancer cells exposed to DNA-PK inhibitor arise from failure of the mitotic machinery to cope with the severe abnormalities in metaphase chromosomes. Misalignment and mis-segregation of damaged/fragmented chromosomes yielded multiple lagging chromosomes and high degree of micronucleation. Cancer cells surviving several days after irradiation in the presence of M3814 had a multinuclear morphology, frequently with fragmented appearance. Numerous MN with intense γH2AX staining indicated a high concentration of unrepaired DSBs. Gene expression analysis of these cells showed a strong activation of inflammatory signaling. Analyses of our data demonstrated a clear correlation between strong STING pathway activation and M3814-induced micronucleation in irradiated A549p53KO cells. In the course of our studies, two independent reports documented a clear mechanistic link between micronucleation and cGAS/STING pathway activation (39, 40). Our results highlight that MN formation is a key mechanism for activation of inflammatory signaling by M3814 and identify DNA-PK inhibition as a powerful generator of inflammatory micronucleation in irradiated p53-deficient cancer cells. In addition, DNA-PK inhibitor substantially enhanced PD-L1 expression in irradiated cancer cells, providing a clear rationale for combination with PD-L1 targeted immunotherapy.

Triple combination of radiation, peposertib, and bintrafusp alfa demonstrated superior efficacy compared with either IR+M3814 or IR+BA in three syngeneic murine tumor models. Addition of M3814 led to complete tumor regression in all MC38 tumor-bearing mice and significant enhancement of activity in the poorly immunogenic B16F10 and immune-excluded 4T1 model. The improved efficacy and survival by M3814 correlated with substantially elevated $CD8^+$ T-cell infiltration in the 4T1 tumors treated with IR, peposertib, and BA, supporting the contribution of the immune system to tumor clearance. These effects were demonstrated in a model system in which BA administration was limited to only three injections within 4 days to minimize mouse immune response to the humanized antibody (31). Such schedule likely underestimates the combination potential in the clinic where radiotherapy and immunotherapy are given over extended periods of time. Nevertheless, even under this suboptimal scheduling, the consistent efficacy boost by M3814 in the triple combination studies supports the hypothesis that DNA-PK inhibitor can serve as a strong immunotherapy enhancer in the clinical setting of combined radio and immunotherapy of locally advanced tumors. This is on top of the demonstrated effective potentiation of radiation-induced cancer cell death in preclinical mouse models (13).

Radiotherapy is a widely used treatment for local or locally advanced malignancies across a wide spectrum of indications (37). However, its effectiveness is limited by normal tissue toxicity. Radiation-induced fibrosis is a debilitating side effect in lung and other normal tissues in the radiation path (41). The mechanisms behind are complex and not completely understood but it is well established that TGFβ signaling plays a key role (41, 42) and it has been identified as a target for pharmacologic intervention (43). Bintrafusp alfa is a bifunctional fusion protein that simultaneously inhibits two nonredundant immunosuppressive pathways, TGFβ and PD-L1 (31). It is composed of the extracellular domain of TGFβRII (TGFβ "trap") fused via a flexible linker to the C-terminus of each heavy chain of an IgG1 antibody blocking PD-L1. It traps TGFβ in the tumor environment and could inhibit its paracrine effects while suppressing PD-1 immune checkpoint blockade, making it a desirable combination partner to any radiosensitizer therapy.

Therapeutic radiation contributes to the generation of cytosolic DNA, activation of the STING pathway, and engagement of antitumor immunity to suppress tumor growth (39, 44, 45). Recent mechanistic

(*Continued.*) **B,** Treatment schedule of combination efficacy studies. For the MC38 model, C57BL/6 mice were inoculated intramuscularly (i.m.) with 0.25 × 106 MC38 cells (day 7) and treated ($n = 10$) with isotype control (133 μg i.v., day 0)+vehicle (0.2 mL orally, every day on days 0–14), BA (164 μg i.v., day 0), IR (3.6 Gy, days 0–3), M3814 (50 mg/kg, orally, every day, days 0–14), IR+BA, BA+M3814, IR+M3814, or IR+M3814+BA. For the B16F10 model, C57BL/6 mice were inoculated i.m. with 1 × 106 B16F10 cells (day 8) and treated ($n = 6$) with isotype control (400 μg i.v., days 0, 2, 4)+vehicle (0.2 mL orally, every day, days 0–14), BA (492 μg i.v., days 0, 2, 4), IR (6 Gy, days 0–3), M3814 (150 mg/kg, orally, every day, days 0–14), IR+BA, BA+M3814, IR+M3814, or IR+M3814. For the 4T1 model, BALB/c mice were inoculated i.m. with 0.5 × 105 4T1 cells (day 6) and treated ($n = 10$) with isotype control (400 μg i.v., days 0, 2, 4)+vehicle (0.2 mL orally, every day, days 0–14), BA (492 μg i.v., days 0, 2, 4), IR (8 Gy, days 0–3), M3814 (150 mg/kg, orally, every day, days 0–14), IR+BA, M3814+BA, IR+M3814, or IR+M3814+BA. **C,** Combination of IR, M3814, and BA enhanced antitumor activity. All tumor volumes were measured twice weekly and presented as mean ± SEM. *P* values were calculated by two-way ANOVA with a Tukey or Sidak post-test. **D,** Combination of IR, M3814, and BA showed superior survival benefit. For survival analysis, mice were sacrificed when tumor volumes reached 2,000 mm^3 and median survival times were calculated. *P* values were calculated by log-rank (Mantel–Cox) tests. **E,** Representative IHC images showing $CD8^+$ T-cell infiltration in 4T1 tumors following therapy (scale bar: 250 μm). BALB/c mice were inoculated i.m. with 0.5 × 105 4T1 cells (day 7) and treated ($n = 12$) with isotype control (400 μg i.v., days 0, 2, 4)+vehicle [0.2 mL, orally, daily (every day), days 0–10], BA (492 μg i.v., days 0, 2, 4), IR (8 Gy, days 0–3), M3814 (150 mg/kg, orally, every day, days 0–10), IR+BA, BA+M3814, IR+M3814, or IR+M3814+BA. 4T1 tumor tissues were harvested at day 10, fixed, and $CD8^+$ cells were detected by IHC. **F,** M3814 enhanced $CD8^+$ T-cell infiltration into 4T1 tumors. The percentage of anti-$CD8^+$ cells as a proportion of total nucleated cells in the 4T1 tumors described in **E** was quantified by HALO analysis and significance was tested by an ordinary one-way ANOVA with Dunnett multiple comparisons test.

insights helped to understand how defects in DNA damage response may lead to accumulation of DSBs and activation of IFN signaling and other immune-related cytokines (39, 40, 46). It is becoming clear that cytosolic DNA exposure is an effective mechanism for activation of the cGAS/STING pathway and the inflammatory response in cancer cells (45, 47, 48). Central to this is the generation of MN emerging from chromosome misalignment and missegregation at the mitotic spindle (21, 39). Their lamin B1-deficient nuclear envelope is prone to rupture and exposes chromosomal material in the cytosol to start the cGAS/STING cascade of events (40). The STING pathway is believed to contribute to the efficacy of radiotherapy and immunotherapy (48, 49). Therefore, STING has emerged as a promising target for activation and several STING agonists are in early stages of development for cancer treatment (50). However, tumor targeted approaches are likely needed because systemic activation of STING signaling may have unwanted consequences, including cytokine storm induction.

Radiotherapy alone causes DSBs, chromosome misalignment/missegregation, MN formation, and cGAS/STING activation. However, these effects are limited because of the relatively rapid repair of DSBs via NHEJ, reducing the number of catastrophic cellular events, MN-containing cells, and the level of IFN signaling. By extending the life of radiation-induced DSBs peposertib treatment allows for a much larger population of cancer cells to enter mitosis with severe chromosome abnormalities, resulting in enhanced cell death, extensive MN formation and strong induction of cGAS/STING signaling in the surviving cancer cells. Therefore, peposertib treatment offers a powerful new way for simultaneous enhancement of cell killing and activation of STING-mediated inflammatory response in irradiated cancer cells. At the same time, due to its unique mechanism of intervening in the cellular response to radiation by overactivation of ATM/p53 signaling axis, DNA-PK inhibitor reinforces p53-dependent protection of proliferating normal cells from mitotic death (15). Peposertib is well tolerated in humans as a single agent (14) and its radiosensitizing effects are limited to a relatively small irradiated body area thus STING activation will likely have limited systemic effect.

Cancer cells with a functional p53 pathway may also benefit from combined radiation and M3814 therapy via a different mechanism where ATM/p53 overactivation reinforces cell-cycle arrest and acquisition of durable premature senescence (15). M3814-induced senescence not only halts cancer cell growth but has the potential to modulate the immune environment via their SASP (51). The senescent p53 wild-type A549 cells generated by the IR+M3814 treatment (15) exhibited activated immune signaling albeit at lower levels than A549p53KO cells (**Fig. 5A** and **D**) without micronucleation (**Fig. 3B** and **C**) and showed immunomodulatory effects that support combination with cancer immunotherapeutic agents (manuscript in preparation). However, the ability of M3814 in p53-negative cells to induce strong cell killing and intense micronucleation, the most efficient mechanism for cGAS/STING activation, in p53-negative cells makes p53-defficient/mutant tumors a preferred choice for triple combination therapy.

Taken together, our studies identified the selective DNA-PK inhibitor peposertib as a powerful enhancer of radiation-induced cGAS/STING signaling and a potential combination partner of bintrafusp alfa in the radioimmunotherapy of p53 dysfunctional cancers. Over 50% of newly diagnosed solid tumors have p53 mutations and this percentage increases with the progression of the disease (52). Planned clinical combination studies of peposertib and bintrafusp alfa in patients undergoing locoregional radiotherapy will be assessing the potential of this novel approach to combined radioimmunotherapy of human cancer.

Authors' Disclosures

M.I. Carr reports all authors, except Y. Guo and A.S. Lazorchak, are employees of Merck KGaA or its affiliate EMD Serono Research and Development Institute, Inc. Merck KGaA and/or its affiliates have certain rights in patents, patent applications pertaining to M3814 (WO 2014/183850 A1), bintrafusp alfa (WO 2015/118175) and a combination of M3814 and bintrafusp alfa (WO2019/211489), with author Y. Lan and C. Xu being named inventors of the latter. L.-Y. Chiu reports all authors, except Y. Guo and A.S. Lazorchak, are employees of Merck KGaA or its affiliate EMD Serono Research and Development Institute, Inc. Merck KGaA and/or its affiliates have certain rights in patents, patent applications pertaining to M3814 (WO 2014/183850 A1), bintrafusp alfa (WO 2015/118175) and a combination of M3814 and bintrafusp alfa (WO2019/211489), with author Y. Lan and C. Xu being named inventors of the latter. C. Xu is an employee of Merck KGaA or its affiliate EMD Serono Research and Development Institute, Inc. Merck KGaA and/or its affiliates have certain rights in patents, patent applications pertaining to M3814 (WO 2014/183850 A1), bintrafusp alfa (WO 2015/118175) and a combination of M3814 and bintrafusp alfa (WO2019/211489), with author Y. Lan and C. Xu being named inventors of the latter. A.S. Lazorchak reports other support from EMD Serono outside the submitted work. B. Marelli is an employee EMD Serono Research and Development Institute, Inc. Merck KGaA and/or its affiliates have certain rights in patents, patent applications pertaining to M3814 (WO 2014/183850 A1), bintrafusp alfa (WO 2015/118175) and a combination of M3814 and bintrafusp alfa (WO2019/211489), with author Y. Lan and C. Xu being named inventors of the latter. Y. Lan reports all authors, except Y. Guo and A.S. Lazorchak, are employees of Merck KGaA or its affiliate EMD Serono Research and Development Institute, Inc. Merck KGaA and/or its affiliates have certain rights in patents, patent applications pertaining to M3814 (WO 2014/183850 A1), bintrafusp alfa (WO 2015/118175) and a combination of M3814 and bintrafusp alfa (WO2019/211489), with author Y. Lan and C. Xu being named inventors of the latter. Q. Sun reports All authors, except Y. Guo and A. Lazorchak, are employees of Merck KGaA or its affiliate EMD Serono Research and Development Institute, Inc. Merck KGaA and/or its affiliates have certain rights in patents, patent applications pertaining to M3814 (WO 2014/183850 A1), bintrafusp alfa (WO 2015/118175) and a combination of M3814 and bintrafusp alfa (WO2019/211489), with author Y. Lan and C. Xu being named inventors of the latter. F. Czauderna reports all authors, except Y. Guo and A.S. Lazorchak, are employees of Merck KGaA or its affiliate EMD Serono Research and Development Institute, Inc. Merck KGaA and/or its affiliates have certain rights in patents, patent applications pertaining to M3814 (WO 2014/183850 A1), bintrafusp alfa (WO 2015/118175) and a combination of M3814 and bintrafusp alfa (WO2019/211489), with author Y. Lan and C. Xu being named inventors of the latter. F.T. Zenke reports all authors, except Y. Guo and A.S. Lazorchak, are employees of Merck KGaA or its affiliate EMD Serono Research and Development Institute, Inc. Merck KGaA and/or its affiliates have certain rights in patents, patent applications pertaining to M3814 (WO 2014/183850 A1), bintrafusp alfa (WO 2015/118175) and a combination of M3814 and bintrafusp alfa (WO2019/211489), with author Y. Lan and C. Xu being named inventors of the latter. A. Blaukat is an employee and minor stock holder of Merck KGaA and all the work described has been funded by Merck KGaA. L.T. Vassilev reports all authors, except Y. Guo and A.S. Lazorchak, are employees of Merck KGaA or its affiliate EMD Serono Research and Development Institute, Inc. Merck KGaA and/or its affiliates have certain rights in patents, patent applications pertaining to M3814 (WO 2014/183850 A1), bintrafusp alfa (WO 2015/118175) and a combination of M3814 and bintrafusp alfa (WO2019/211489), with author Y. Lan and C. Xu being named inventors of the latter. No disclosures were reported by the other authors.

Authors' Contributions

M.I. Carr: Conceptualization, resources, data curation, formal analysis, supervision, investigation, methodology, writing–original draft, project administration. **L.-Y. Chiu:** Conceptualization, data curation, formal analysis, investigation, visualization, methodology, writing–original draft. **Y. Guo:** Conceptualization, data curation, formal analysis, investigation, visualization, methodology, writing–original draft. **C. Xu:** Conceptualization, data curation, formal analysis, validation, investigation, methodology. **A.S. Lazorchak:** Conceptualization, data curation, formal analysis, validation, investigation, methodology, writing–original draft. **H. Yu:** Conceptualization, data curation, formal analysis, investigation, methodology, writing–original draft. **G. Qin:** Data curation, investigation. **J. Qi:** Data curation, investigation. **B. Marelli:** Data curation, formal analysis, validation, investigation. **Y. Lan:** Conceptualization, data curation, formal analysis, supervision, validation, investigation. **Q. Sun:** Conceptualization, data curation, formal analysis, supervision, validation, investigation, methodology. **F.T. Czauderna:** Data curation, investigation, methodology. **F.T. Zenke:** Conceptualization,

resources, methodology, project administration, writing–review and editing. **A. Blaukat:** Conceptualization, resources, project administration, writing–review and editing. **L.T. Vassilev:** Conceptualization, resources, formal analysis, supervision, investigation, writing–original draft, project administration, writing–review and editing.

Acknowledgments

This research was funded by Merck KGaA. All authors are employees of Merck KGaA or its affiliate EMD Serono Research and Development Institute, Inc. We thank Xiaohong Liu for the insightful discussions and Florian Szardenings for his helpful comments.

The costs of publication of this article were defrayed in part by the payment of page charges. This article must therefore be hereby marked *advertisement* in accordance with 18 U.S.C. Section 1734 solely to indicate this fact.

Received July 29, 2021; revised November 9, 2021; accepted December 21, 2021; published first January 3, 2022.

References

1. Salles B, Calsou P, Frit P, Muller C. The DNA repair complex DNA-PK, a pharmacological target in cancer chemotherapy and radiotherapy. Pathol Biol 2006;54:185–93.
2. Curtin NJ. DNA repair dysregulation from cancer driver to therapeutic target. Nat Rev Cancer 2012;12:801–17.
3. Brown JS, O'Carrigan B, Jackson SP, Yap TA. Targeting DNA repair in cancer: beyond PARP inhibitors. Cancer Discov 2017;7:20–37.
4. Beucher A, Birraux J, Tchouandong L, Barton O, Shibata A, Conrad S, et al. ATM and Artemis promote homologous recombination of radiation-induced DNA double-strand breaks in G2. EMBO J 2009;28:3413–27.
5. Blackford AN, Jackson SP. ATM, ATR, and DNA-PK: the trinity at the heart of the DNA damage response. Mol Cell 2017;66:801–17.
6. Hiom K. Coping with DNA double strand breaks. DNA Repair 2010;9:1256–63.
7. Kasparek TR, Humphrey TC. DNA double-strand break repair pathways, chromosomal rearrangements and cancer. Semin Cell Dev Biol 2011;22:886–97.
8. Davis AJ, Chen DJ. DNA double strand break repair via non-homologous end-joining. Transl Cancer Res 2013;2:130–43.
9. Lee SH, Kim CH. DNA-dependent protein kinase complex: a multifunctional protein in DNA repair and damage checkpoint. Mol Cells 2002;13:159–66.
10. Jette N, Lees-Miller SP. The DNA-dependent protein kinase: a multifunctional protein kinase with roles in DNA double strand break repair and mitosis. Prog Biophys Mol Biol 2015;117:194–205.
11. Dobbs TA, Tainer JA, Lees-Miller SP. A structural model for regulation of NHEJ by DNA-PKcs autophosphorylation. DNA Repair 2010;9:1307–14.
12. Furgason JM, Bahassi el M. Targeting DNA repair mechanisms in cancer. Pharmacol Ther 2013;137:298–308.
13. Zenke FT, Zimmermann A, Sirrenberg C, Dahmen H, Kirkin V, Pehl U, et al. Pharmacological inhibitor of DNA-PK, M3814, potentiates radiotherapy and regresses human tumors in mouse models. Mol Cancer Ther 2020;19:1091–101.
14. van Bussel MTJ, Awada A, de Jonge MJA, Mau-Sørensen M, Nielsen D, Schöffski P, et al. A first-in-man phase 1 study of the DNA-dependent protein kinase inhibitor peposertib (formerly M3814) in patients with advanced solid tumours. Br J Cancer 2021;124:728–35.
15. Sun Q, Guo Y, Liu X, Czauderna F, Carr MI, Zenke FT, et al. Therapeutic implications of p53 status on cancer cell fate following exposure to ionizing radiation and the DNA-PK inhibitor M3814. Mol Cancer Res 2019;17:2457–68.
16. Kanda T, Sullivan KF, Wahl GM. Histone-GFP fusion protein enables sensitive analysis of chromosome dynamics in living mammalian cells. Curr Biol 1998;8:377–85.
17. Ruf-Zamojski F, Ge Y, Pincas H, Shan J, Song Y, Hines N, et al. Cytogenetic, genomic, and functional characterization of pituitary gonadotrope cell lines. J Endocr Soc 2019;3:902–20.
18. Scheffner M, Huibregtse JM, Vierstra RD, Howley PM. The HPV-16 E6 and E6-AP complex functions as a ubiquitin-protein ligase in the ubiquitination of p53. Cell 1993;75:495–505.
19. Stevens JB, Liu G, Bremer SW, Ye KJ, Xu W, Xu J, et al. Mitotic cell death by chromosome fragmentation. Cancer Res 2007;67:7686–94.
20. Santaguida S, Amon A. Short- and long-term effects of chromosome mis-segregation and aneuploidy. Nat Rev Mol Cell Biol 2015;16:473–85.
21. Bakhoum SF, Kabeche L, Murnane JP, Zaki BI, Compton DA. DNA-damage response during mitosis induces whole-chromosome missegregation. Cancer Discov 2014;4:1281–9.
22. Simons A, Shaffer LG, Hastings RJ. Cytogenetic nomenclature: changes in the ISCN 2013 compared to the 2009 edition. Cytogenet Genome Res 2013;141:1–6.
23. Crasta K, Ganem NJ, Dagher R, Lantermann AB, Ivanova EV, Pan Y, et al. DNA breaks and chromosome pulverization from errors in mitosis. Nature 2012;482:53–8.
24. Vassilev LT, Tovar C, Chen S, Knezevic D, Zhao X, Sun H, et al. Selective small-molecule inhibitor reveals critical mitotic functions of human CDK1. Proc Natl Acad Sci U S A 2006;103:10660–5.
25. Hatch EM, Fischer AH, Deerinck TJ, Hetzer MW. Catastrophic nuclear envelope collapse in cancer cell micronuclei. Cell 2013;154:47–60.
26. Yang H, Wang H, Ren J, Chen Q, Chen ZJ. cGAS is essential for cellular senescence. Proc Natl Acad Sci U S A 2017;114:E4612–20.
27. El-Deiry WS. p21(WAF1) mediates cell-cycle inhibition, relevant to cancer suppression and therapy. Cancer Res 2016;76:5189–91.
28. Ma F, Li B, Yu Y, Iyer SS, Sun M, Cheng G. Positive feedback regulation of type I interferon by the interferon-stimulated gene STING. EMBO Rep 2015;16:202–12.
29. Sato H, Niimi A, Yasuhara T, Permata TBM, Hagiwara Y, Isono M, et al. DNA double-strand break repair pathway regulates PD-L1 expression in cancer cells. Nat Commun 2017;8:1751.
30. Akinleye A, Rasool Z. Immune checkpoint inhibitors of PD-L1 as cancer therapeutics. J Hematol Oncol 2019;12:92.
31. Lan Y, Zhang D, Xu C, Hance KW, Marelli B, Qi J, et al. Enhanced preclinical antitumor activity of M7824, a bifunctional fusion protein simultaneously targeting PD-L1 and TGF-β. Sci Transl Med 2018;10:eaan5488.
32. Stone HB, Coleman CN, Anscher MS, McBride WH. Effects of radiation on normal tissue: consequences and mechanisms. Lancet Oncol 2003;4:529–36.
33. Straub JM, New J, Hamilton CD, Lominska C, Shnayder Y, Thomas SM. Radiation-induced fibrosis: mechanisms and implications for therapy. J Cancer Res Clin Oncol 2015;141:1985–94.
34. Bouquet F, Pal A, Pilones KA, Demaria S, Hann B, Akhurst RJ, et al. TGFβ1 inhibition increases the radiosensitivity of breast cancer cells in vitro and promotes tumor control by radiation in vivo. Clin Cancer Res 2011;17:6754–65.
35. Lechner MG, Karimi SS, Barry-Holson K, Angell TE, Murphy KA, Church CH, et al. Immunogenicity of murine solid tumor models as a defining feature of in vivo behavior and response to immunotherapy. J Immunother 2013;36:477–89.
36. Harrington KJ, Billingham LJ, Brunner TB, Burnet NG, Chan CS, Hoskin P, et al. Guidelines for preclinical and early phase clinical assessment of novel radiosensitisers. Br J Cancer 2011;105:628–39.
37. Baumann M, Krause M, Overgaard J, Debus J, Bentzen SM, Daartz J, et al. Radiation oncology in the era of precision medicine. Nat Rev Cancer 2016;16:234–49.
38. Begg AC, Stewart FA, Vens C. Strategies to improve radiotherapy with targeted drugs. Nat Rev Cancer 2011;11:239–53.
39. Harding SM, Benci JL, Irianto J, Discher DE, Minn AJ, Greenberg RA. Mitotic progression following DNA damage enables pattern recognition within micronuclei. Nature 2017;548:466–70.
40. Mackenzie KJ, Carroll P, Martin CA, Murina O, Fluteau A, Simpson DJ, et al. cGAS surveillance of micronuclei links genome instability to innate immunity. Nature 2017;548:461–5.
41. Käsmann L, Dietrich A, Staab-Weijnitz CA, Manapov F, Behr J, Rimner A, et al. Radiation-induced lung toxicity - cellular and molecular mechanisms of pathogenesis, management, and literature review. Radiat Oncol 2020;15:214.
42. Barcellos-Hoff MH, Cucinotta FA. New tricks for an old fox: impact of TGFβ on the DNA damage response and genomic stability. Sci Signal 2014;7:re5.
43. Colak S, Ten Dijke P. Targeting TGF-β signaling in cancer. Trends Cancer 2017;3:56–71.
44. Deng L, Liang H, Burnette B, Beckett M, Darga T, Weichselbaum RR, et al. Irradiation and anti-PD-L1 treatment synergistically promote antitumor immunity in mice. J Clin Invest 2014;124:687–95.

45. Deng L, Liang H, Xu M, Yang X, Burnette B, Arina A, et al. STING-dependent cytosolic DNA sensing promotes radiation-induced type i interferon-dependent antitumor immunity in immunogenic tumors. Immunity 2014; 41:843–52.
46. Glück S, Guey B, Gulen MF, Wolter K, Kang TW, Schmacke NA, et al. Innate immune sensing of cytosolic chromatin fragments through cGAS promotes senescence. Nat Cell Biol 2017;19:1061–70.
47. Ishikawa H, Ma Z, Barber GN. STING regulates intracellular DNA-mediated, type I interferon-dependent innate immunity. Nature 2009; 461:788–92.
48. Kwon J, Bakhoum SF. The cytosolic DNA-sensing cGAS-STING pathway in cancer. Cancer Discov 2020;10:26–39.
49. Reisländer T, Groelly FJ, Tarsounas M. DNA damage and cancer immunotherapy: a STING in the tale. Mol Cell 2020;80:21–8.
50. Berger G, Marloye M, Lawler SE. Pharmacological modulation of the STING pathway for cancer immunotherapy. Trends Mol Med 2019;25:412–27.
51. Muñoz-Espín D, Serrano M. Cellular senescence: from physiology to pathology. Nat Rev Mol Cell Biol 2014;15:482–96.
52. Olivier M, Hollstein M, Hainaut P. TP53 mutations in human cancers: origins, consequences, and clinical use. Cold Spring Harb Perspect Biol 2010;2:a001008.